Effect of Processing Atmosphere and Secondary Operations on the Mechanical Properties of Additive Manufactured AISI 316L Stainless Steel by Plasma Metal Deposition

Cristina Arévalo [1] [iD]**, Enrique Ariza** [2] [iD]**, Eva Maria Pérez-Soriano** [1,*] [iD]**, Michael Kitzmantel** [2]**, Erich Neubauer** [2] **and Isabel Montealegre-Meléndez** [1] [iD]

[1]   Escuela Politécnica Superior, Universidad de Sevilla, 41011 Sevilla, Spain; carevalo@us.es (C.A.); imontealegre@us.es (I.M.-M.)

[2]   RHP-Technology GmbH, 2444 Seibersdorf, Austria; e.ar@rhp.at (E.A.); m.ki@rhp.at (M.K.); e.ne@rhp.at (E.N.)

[*]   Correspondence: evamps@us.es; Tel.: +34-954482278

check for updates

Abstract: Plasma metal deposition (PMD) is an interesting additive technique whereby diverse materials can be employed to produce end parts with complex geometries. This study investigates not only the effects of the manufacturing conditions on the final properties of 316L stainless steel specimens by PMD, but it also affords an opportunity to study how secondary treatments could modify these properties. The tested processing condition was the atmosphere, either air or argon, with the other parameters having previously been optimized. Furthermore, two standard thermal treatments were conducted with the intention of broadening knowledge regarding how these secondary operations could cause changes in the microstructure and properties of 316L parts. To better appreciate and understand the variation of conditions affecting the behavior properties, a thorough characterization of the specimens was carried out. The results indicate that the presence of vermicular ferrite (δ) varied slightly as a consequence of the processing conditions, since it was less prone to appear in specimens manufactured in argon than in air. In this respect, their mechanical properties suffered variations; the higher the ferrite (δ) content, the higher the mechanical properties measured. The degree of influence of the thermal treatment was similar regardless of the processing conditions, which affected the properties based on the heating temperature.

Keywords: plasma metal deposition; additive manufacturing; 316L; processing conditions; mechanical properties; microstructure

1. Introduction

Nowadays, several additive manufacturing (AM) processes are employed in diverse industrial sectors as recognized techniques to produce specimens with determined and specific geometries [1,2]. These well-known techniques involve layer-by-layer shaping and building components [3] in opposition to the conventional manufacturing techniques, in which the parts are built in bulk [4]. In the framework of the AM processes in the field of metals, their general classification could be carried out while considering the two different feedstock systems: powder–bed and injection deposition techniques [5]. The technology of the powder–bed processes enables parts to be built with complex geometric shapes; however, the building volumes may be limited to small components [6]. Components of a larger volume can be produced by injection deposition techniques, whereby shapes and geometries often demand a lower degree of complexity [7]. The technologies of injection deposition can be broadly classified into powder and wire systems, in which the starting materials could be fed or blown [1].

The technology of a wire-fed system is faster than the other techniques, thereby allowing a high production rate [8]. However, this process is limited by the availability of raw materials. Laser and plasma metal deposition (LMD & PMD) are included in the category of blown powder techniques.

The PMD manufacturing process is a rapidly rising AM technology thanks to its advantages over laser-based AM processes. In this technique, a plasma is used as the energy source to melt the starting materials [9,10]. The plasma spot, larger than the laser spot, presents a high feeding rate (1–10 kg/h) and, as a consequence, a high production rate, which is interesting for today's industrial sector [11,12]. Moreover, it is not limited by the feedstock material weight or component size as in powder–bed systems since the plasma torch is attached to a Gantry system and the deposition is performed on a workbench of the desired size. Currently, PMD is used in the prototype scale [13], as well as for structural components [14]. Due to the high energy delivered to the feedstock deposited on a substrate, a melt pool is generated; simultaneously, an inert gas is blown. Such an inert gas aids in the injection of the powder feed and also protects the formed components from oxidation. Thus, the specimen is produced layer-by-layer. Finally, the three-dimensional component is built. Concerning the deposition process and the feedstock melting, the consolidated material on the substrate may be involved in the reheating cycles, which could promote variations on the microstructure and changes in the final component behavior. Several authors describe the importance of a thorough understanding of the relevant parameters, not only regarding the starting powder (flow rate, size, shape, composition, etc.), but also the processing conditions (transferred arc, speed, atmospheric conditions, etc.) [10,15]. Therefore, the influence of these significant parameters should be considered on the final properties of the components.

In AM technology, 316L stainless steel powder is commonly employed to develop complex geometries since this alloy presents attractive properties for many industrial sectors, such as highly resistant corrosion behavior and toughness [16]. Previous authors indicate that the microstructure of this austenitic stainless steel could suffer variations as a consequence of the manufacturing process. Retained δ-ferrite phase with various morphologies and intermetallic σ triggered by the replacement of δ, could be present in the microstructure in addition to the expected γ-austenite phase. This may be related to the processing parameters and ambient conditions in which the parts are built; in this regard, the final mechanical and tribological properties of the components could be affected [17–20].

The peculiarities of this innovative PMD process, such as its fast heating/cooling rates, could result in remarkably different microstructures compared with traditional fabrication routes, such as casting. In other additive techniques, such as selective laser melting (SLM), many authors state the benefits of AM and how the optimization of fabrication parameters presents a positive effect on the final properties of the specimens [21–24]. Moreover, these investigations reveal that there would be a direct relationship between the final microstructure and the properties with the number of layers; it is suggested that the microstructure could be influenced by the accumulated heat which would lead to the non-equilibrium microstructure. Secondary thermal treatments are carried out in order to improve the final properties [25], and their effect on the microstructure is studied.

In this work, the importance of the ambient condition during the PMD process is studied through the manufacture of two walls made from powders of 316L stainless steel, built in air and argon, respectively. Furthermore, two standard thermal treatments are performed in selected specimens extracted from each wall, to evaluate possible variations in their final properties. In this context, this research is intended to deepen and broaden scientific knowledge on how ambient conditions and the secondary treatments affect the properties and the microstructure of the PMD specimens.

2. Materials and Methods

2.1. Materials

The starting powder studied in this research was AISI 316L stainless steel, produced by the water-atomization method, leading to a particle size range of 75–150 μm. This powder was supplied by the Hoeganaes Corporation (Radevorwald, Germany).

The feedstock was chemically analyzed to confirm the composition and compare it to the standard composition. For this purpose, a scanning electron microscope equipped with an energy dispersion X-ray spectroscopy detector (SEM/EDS Hitachi TM1000, Tokyo, Japan) was used; the results are listed in Table 1. Additionally, a particle morphology analysis was carried out via optical microscopy (Figure 1a, OM, Zeiss ICM 405, ZEISS Invers LM, Oberkochen, Germany) and SEM (Figure 1b,c). The morphology appeared to be irregular with rounded edges. In Figure 1a, some internal porosity can be observed.

Table 1. Chemical composition of the standard 316L and the starting powder employed as feedstock.

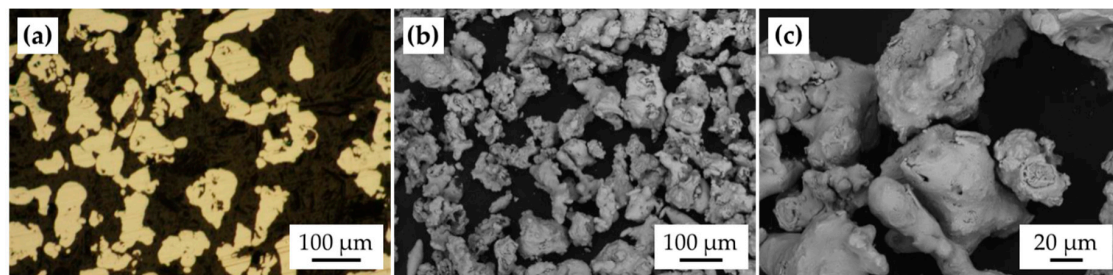| SOURCE INFO	Composition in Mass%								
	Fe	Cr	Ni	Mo	Mn	Si	P	S	C
Hoeganaes Corporation	Bal.	16.37	12.78	2.22	0.07	0.84	0.019	0.002	0.015
EDS Analysis	Bal.	23.5	6.8	0.6	–	0.6	–	–	–
Standard [26]	Bal.	18–16	14–10	3–2	max. 2	max. 0.75	max. 0.045	max. 0.03	max. 0.03

Figure 1. Microscopy analysis of the feedstock. (**a**) optical microscopy (OM) image of the cross-section of the starting particles of 316L; (**b**,**c**) SEM images of the powder particles.

X-ray diffraction (XRD) analysis was conducted by Bruker D8 Advance A25 equipment (Bruker, Billerica, MA, USA) with Cu-K$_\alpha$ radiation. In Figure 2, the X-ray pattern reveals the significant peaks of the γ phase of the 316L stainless steel.
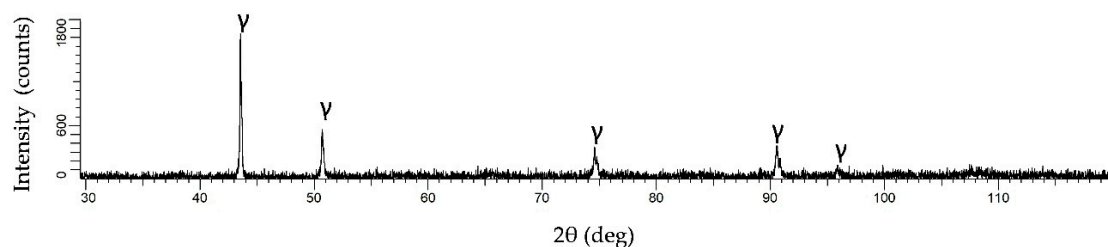

Figure 2. XRD analysis of the starting powder.

2.2. Plasma Metal Deposition Process

Samples were manufactured via a PMD technique which employed an argon plasma as an energy source for melting the starting material in powder, injected directly in the plasma torch. The PMD device was mounted on a 2.5-axis CNC machine; both types of equipment are the property of RHP-Technology GmbH.

A commercial AISI 1015 steel plate with dimensions of 200 mm × 200 mm × 10 mm was selected as substrate. As on previous authors' work [9,15], the feasibility of manufacturing the raw material powders by PMD processing was tested by optimizing the following welding parameters: main arc current (A), pilot current (A), welding speed (mm/min), material feeding rate (g/min), pilot gas flow (L/min) and shielding gas flow (L/min). The parameter optimization was carried out in order to avoid cracks, delamination between layers due to a lack of input energy and porosity as a result of gas trapped in the matrix when high energy is used.

Two walls of 150 mm × 40 mm × 15 mm in size were produced by an oscillation movement: one wall was manufactured in open atmosphere condition (see Figure 3a), using a local shielding gas only as a protective agent against oxidation; while the second wall was fabricated inside a hermetic box filled with argon as the inert atmosphere (see Figure 3b), which protected the entire wall from oxidation during the whole process. In this regard, the influence of the ambient condition was evaluated on the final behavior of the specimens.
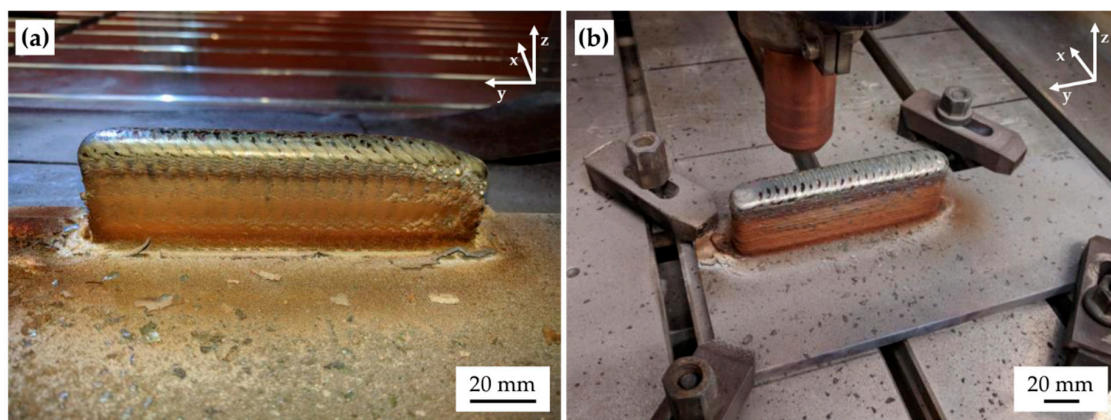

Figure 3. Images of the fabricated walls. (**a**) W1, produced in air atmosphere; (**b**) W2, produced in argon protective atmosphere.

The optimized manufacturing parameters selected to fabricate both walls are shown in Table 2.

Table 2. Processing parameters of plasma metal deposition (PMD) 316L.

Main Current (A)	Pilot Current (A)	Oscillation Welding Speed (mm/min)	Material Feeding Rate (g/min)	Pilot Gas Flow (L/min)
130	35	600	16.2	1.5

In the context of the manufacturing conditions, for the open atmosphere wall (W1), an argon shielding gas flow of 15 L/min was used; on the other hand, for the inert atmosphere test wall (W2), no shielding gas was employed since the hermetic box was filled with argon to control the oxygen below 50 ppm.

2.3. Sample Extraction and Thermal Treatments

Three different sets of tensile test samples were extracted by an electro discharge machining (EDM) Mitsubishi DWC 110 (Mitsubishi, Tokyo, Japan). The dimensions of the extracted specimens were in accordance with the standard [27]. Their geometry and their location in the walls are shown in Figure 4.
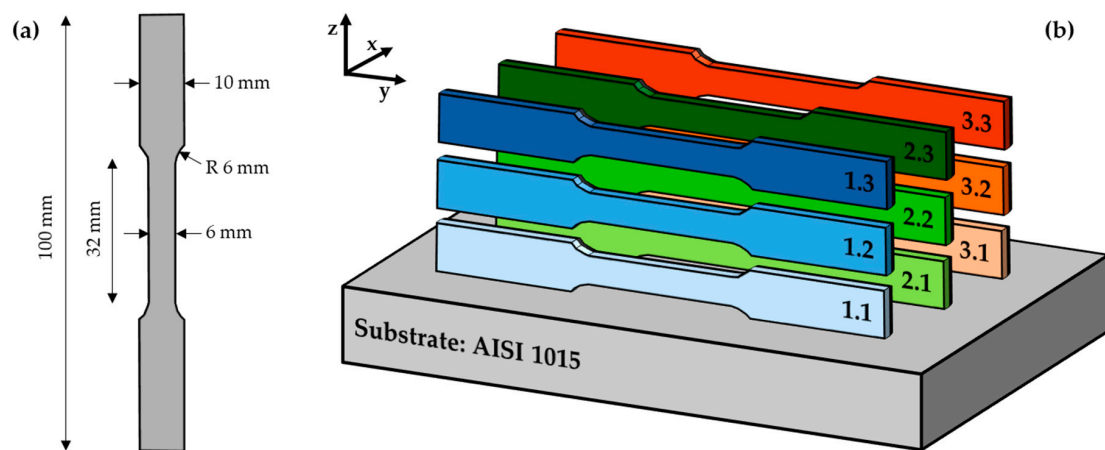
Figure 4. Schematic images of (**a**) a tensile test sample with its dimensions and (**b**) the numbering of the samples for the tensile tests and their location in the walls: (**b.1**) 1.1, 1.2, 1.3 as-built specimens; (**b.2**) 2.1, 2.2, 2.3 specimens treated by TT1; and (**b.3**) 3.1, 3.2, 3.3 specimens treated by TT2.

Following the investigation of the as-built specimens, the thermal treatments were performed using a high vacuum vertical tube furnace model APF-0716-MM (Thermal Technology GmbH, Bayreuth, Germany) under argon atmosphere. The thermal treatment parameters were selected based on the existing literature [26,28]; these are listed in Table 3. The treatment named TT1 involved an enhancement of the temperature only up to 600 °C (stress relief); in the treatment named TT2, in contrast, the heating was carried out at 950 °C (austenitization). The postprocessing parameters of 10 °C/min as the heating rate, 2 h for holding time and 10 °C/min as the cooling rate were the same for both processes; the heating temperature was the crucial factor to induce possible changes in the treated specimens.

Table 3. Thermal treatments performed on the two sets of 316L tensile test specimens, for both cases of air and argon atmosphere manufacturing, along with the sample identification.

Thermal Treatment	Thermal Treatment Cycle	Samples Location in Wall (Figure 4)
As built	–	1.1, 1.2, 1.3
TT1	10 °C/min, 600 °C, 2 h, 10 °C/min, RT	2.1, 2.2, 2.3
TT2	10 °C/min, 950 °C, 2 h, 10 °C/min, RT	3.1, 3.2, 3.3

2.4. Microstructural Characterization and Mechanical and Tribological Behavior

A detailed characterization was conducted in this research. The microstructural study was performed, after metallographic preparation, with a Nikon Epiphot optical microscope (Nikon, Tokyo, Japan) and a scanning electron microscope (FEI Teneo, Hillsboro, OR, USA) equipped with an EDS system to carry out compositional analysis and elemental mapping.

The Archimedes' method [29] enabled the density to be determined for the different sets of specimens. Image analysis (IA) was performed with a Nikon Epiphot optical microscope (Nikon, Tokyo, Japan) coupled with a Jenoptik Progres C3 camera (Jenoptik, Jena, Germany) and then processed using Image-Pro Plus 6.2 software (Media Cybernetics, Bethesda, MD, USA). Struers-Duramin A300 (Ballerup, Germany) was employed to reach the Vickers hardness (HV2). The hardness measurements took place on the polished cross-section of both walls.

Macro mechanical characterization was carried out through tensile tests by employing an Instron 5505-load unit (Norwood, MA, USA) using a strain rate of 0.5 mm·min^{-1} at room temperature. The mechanical properties under study were ultimate tensile strength (UTS), yield strength (YS, σ_y), Young's modulus (E) and elongation (ε).

An instrumented microindentation device, MTR3/50-50/NI (Microtest, Madrid, Spain), was employed on samples to evaluate their micromechanical behavior. The Vickers pyramid diamond tip was set in the simple loading/unloading mode. The resulting load–penetration (P–h) curves were measured using the Oliver and Pharr analysis [30], and the elastic relaxation values were calculated. Six indentations were made for each sample: three for a maximum load of 1 N and three for 5 N (load rate of 1 N/min and 5 N/min, respectively), with a holding time of 40 s.

After macro- and micromechanical characterization, the tribological behavior of the samples was ascertained by a ball-on-disc tribometer (Microtest MT/30/NI, Madrid, Spain). Ceramic alumina balls of 6 mm in diameter were employed. Moreover, for running the tests, the specimens were grounded, polished, cleaned with acetone in an ultrasonic bath, and, as a last step, dried. The tests were carried out under the following parameters: room temperature, a normal load of 5 N on the ball and a 200 rpm sliding speed for 15 min on a circular path of 2-mm radius. The worn surface morphology was studied by optical microscopy (OM) with a Leica Zeiss DMV6 (Leica Microsystems, Heerbrugg, Switzerland).

3. Results

The results were studied and compared in accordance with the manufacturing atmosphere condition, air and argon, in addition to the as-built specimens or the thermal treatments, TT1 and TT2, performed on specific specimens, as described above.

3.1. Microstructure

The microstructural characterization confirmed the existence of an austenite (γ) matrix in all the specimens, regardless of the processing conditions and the thermal treatment, as expected [25]. The retained ferrite (δ) was also present and exhibited a fine vermicular morphology. There were slight differences in how this phase appeared depending on the atmosphere conditions and the postprocessing treatment carried out (Figure 5).
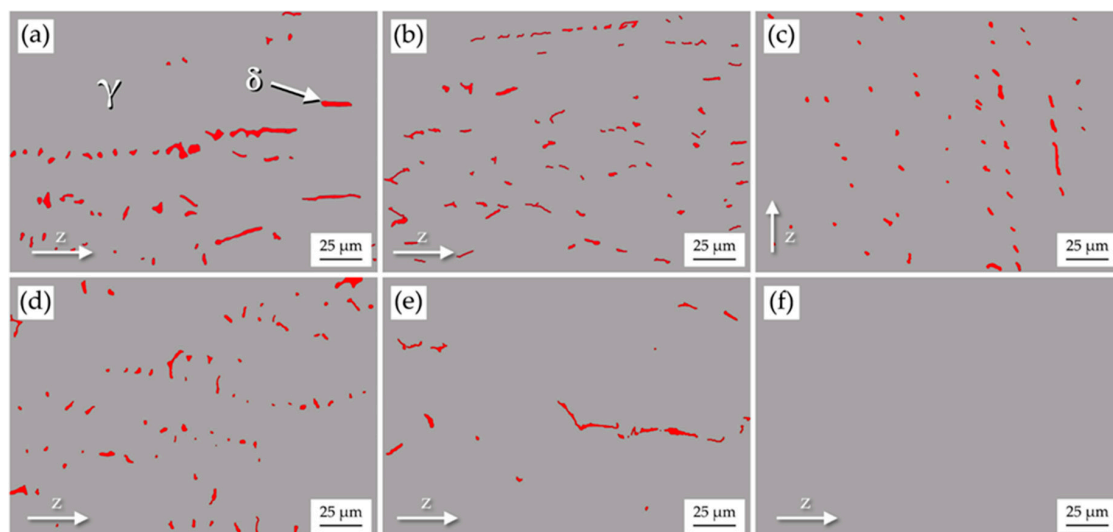

Figure 5. Processed OM images from the following specimens. (**a**) air-1.1; (**b**) air-2.2; (**c**) air-3.3; (**d**) argon-1.1; (**e**) argon-2.2; and (**f**) argon-3.3.

Observing the microstructure of the processed specimens, δ grew as a dendritic morphology [18] along with the vertical direction of the wall (z). The austenite phase was formed around the boundaries of the ferrite; therefore, γ seems to be oriented within the dendrites. This orientation (z) was more noticeable in air (see Figure 5a) than in argon (see Figure 5d). In the case of the specimens manufactured in argon, there was a soft phase orientation. Furthermore, the content of this ferrite was slightly

reduced when the specimens were processed in argon, regardless of the thermal treatment, as can be qualitatively appreciated in Figure 5.

From the point of view of the postprocessing, both thermal treatments resulted in decreasing the vermicular phase while maintaining a similar tendency in its occurrence on the basis of the aforementioned air and argon conditions. TT2 caused a greater decrement of the ferrite than did TT1. This trend was more significant in specimens processed in argon than in specimens fabricated in the air condition, as can clearly be observed when the microstructures shown in Figure 5c,f are compared.

In a detailed evaluation of the microstructure of specimens located in determinate positions, several differences could be appreciated. Regarding the specimens that were extracted from the top and the base of the walls, argon-1.3 and argon-1.1, respectively, the content of the vermicular phase was similar; however, the specimens cut from the center of the walls, argon-1.2, presented a slightly lower content of ferrite (δ). This suggests that the heat dissipation on the center was less pronounced than in the areas close to the substrate and the top. In this regard, a low rate of heat dissipation during the manufacturing process contributed towards the disaggregation and transformation of the retained vermicular phase [18,31,32]. This phenomenon is shown in Figure 6.
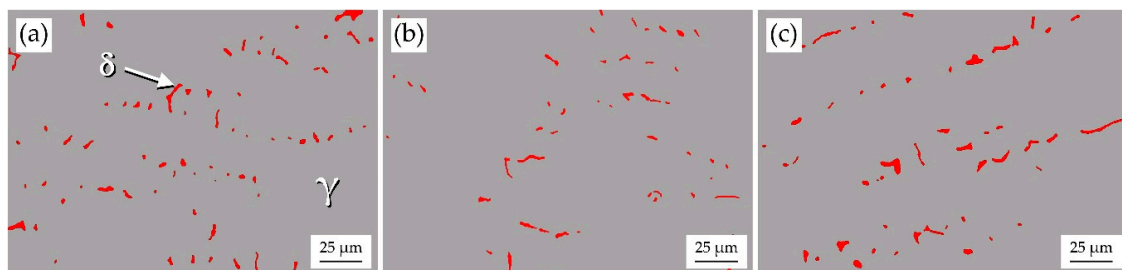

Figure 6. Processed OM images from the following specimens. (**a**) argon-1.1; (**b**) argon-1.2; and (**c**) argon-1.3.

In order to confirm the elemental content of the various phases, three specific points were analyzed using a circular backscatter (CBS-) SEM with EDS for sample air-1.1 (Figure 7). Spot 1, marked in Figure 7, shows the lowest content of chromium, with this point set in the austenite matrix. For Spot 3, the concentration of chromium lightly increased; and the highest content of chromium was measured at Spot 2; in both these latter spots, the vermicular morphology could be identified. These EDS analyses suggest that the vermicular phase is rich in chromium and also in molybdenum, while the matrix (Spot 1) presents more nickel content than in the vermicular phase.

Furthermore, a compositional mapping was carried out in sample argon-2.2 in order to verify the elemental distribution. Figure 8 confirms the presence of chromium and molybdenum in the vermicular areas; both elements appeared in the δ-ferrite phase in a higher content than in the austenite matrix.

It should be borne in mind that the vermicular δ phase may embed the intermetallic σ phase that commonly possesses the highest content of chromium and molybdenum [25]. In accordance with previous authors, this σ phase arises from the decomposition of the δ phase. Therefore, the identification of this intermetallic may relate to the presence of the vermicular areas. Figure 9a shows a higher-magnification SEM image that enabled the detection of the intermetallic σ. There were small amounts of this phase embedded in the vermicular ferrite areas and preferably placed in the gamma-delta ferrite interphase. More intermetallic sigma phase can be found in as-built samples, in the central position of the walls [18]. These regions can also be observed in OM (Figure 9b).
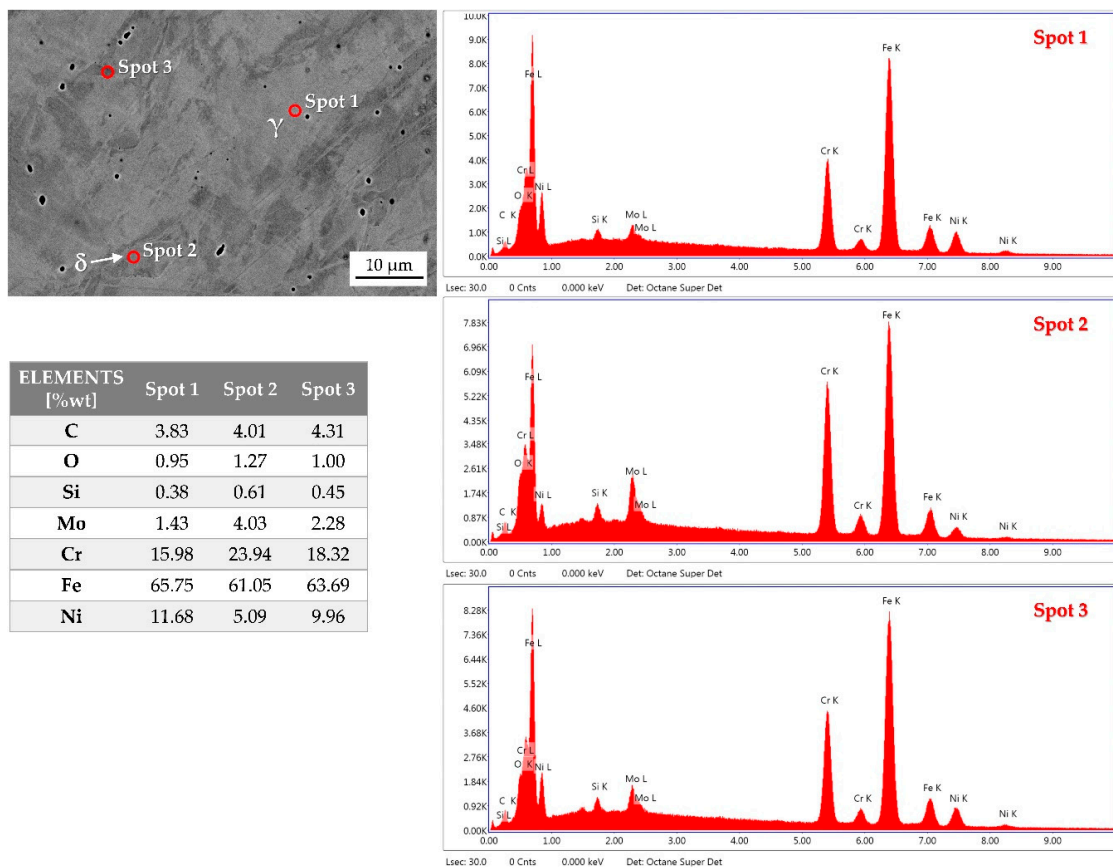
ELEMENTS [%wt]	Spot 1	Spot 2	Spot 3
C	3.83	4.01	4.31
O	0.95	1.27	1.00
Si	0.38	0.61	0.45
Mo	1.43	4.03	2.28
Cr	15.98	23.94	18.32
Fe	65.75	61.05	63.69
Ni	11.68	5.09	9.96

Figure 7. EDS–SEM image and the analysis of three spots in sample air-1.1.
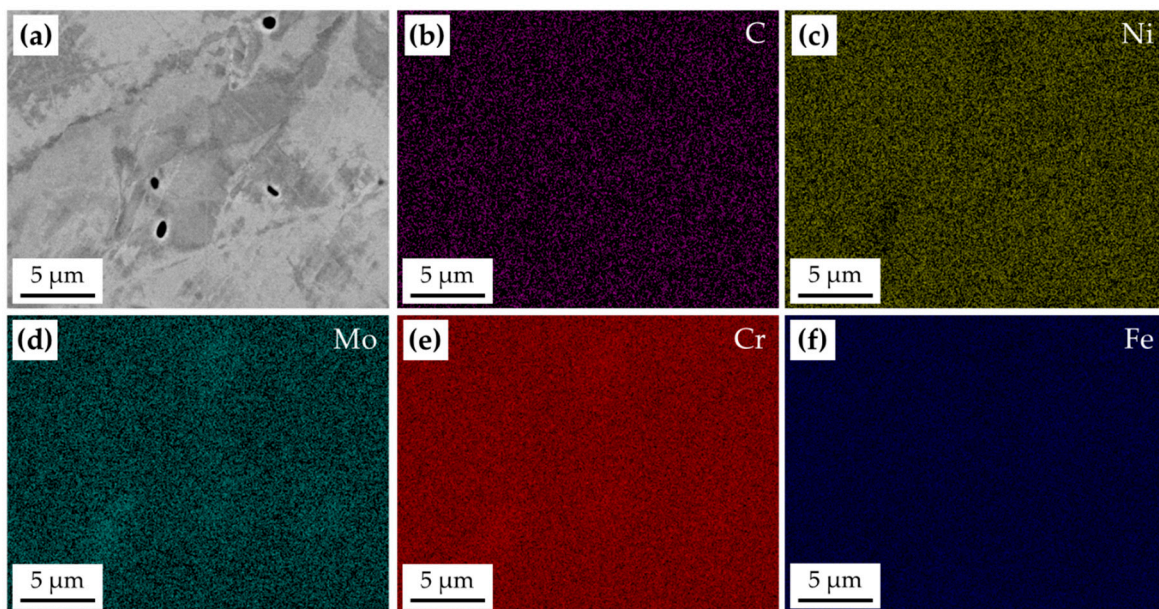
Figure 8. Compositional mapping of sample argon-2.2. (**a**) SEM image; (**b**) carbon; (**c**) nickel; (**d**) molybdenum; (**e**) chromium; and (**f**) iron.
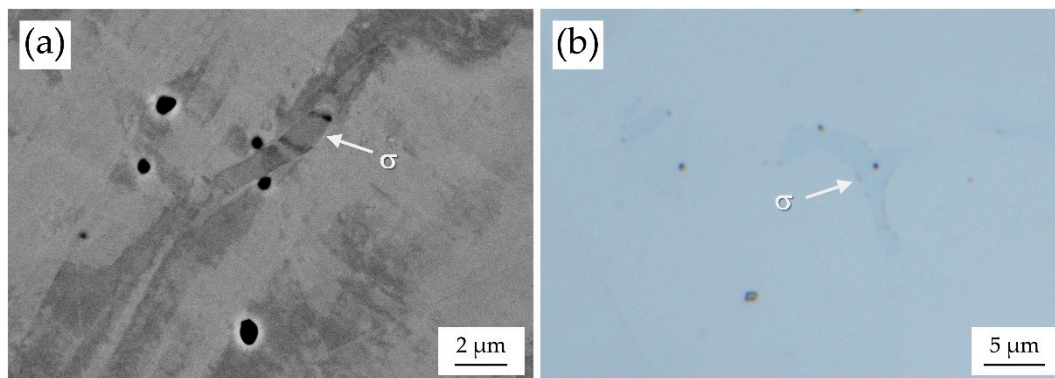
Figure 9. Identification of intermetallic σ phase. (**a**) CBS–SEM image from sample air-1.2; and (**b**) OM image from sample argon-1.2.

3.2. Mechanical Properties

In general terms, AISI 316L stainless steel specimens processed by PMD were dense with porosity values lower than 1%, obtained by IA and densification by the Archimedes' method.

Concerning hardness, a whole wall section was measured along with the height. The obtained results were similar within each wall. The average hardness values were 150 HV in air and 140 HV in argon. Therefore, in both cases, the achieved hardness was slightly reduced from the nominal values, but similar to the typical results from metal deposition techniques (140–175 HV) [18,28,33,34].

In the context of the mechanical properties measurements, the tensile test results were studied and compared on the basis of: (i) ultimate tensile strength (UTS), (ii) elongation (ε), (iii) yield strength (YS) and (iv) Young's modulus (E). A comparative study was performed, not only to achieve the effect of the manufacturing conditions in the final behavior of the specimens (air and argon), but also to comprehend the influence of the thermal treatment applied. Figures 10–12 provide data on the average calculated values after the testing of three specimens located in the three different positions shown in Figure 4.

A graphic depiction of the average properties of the as-built specimens studied can be observed in Figure 10. The goodness of selected manufacturing parameters was verified since the UTS, ε, and YS achieved values close to the standard values (450 MPa, 40% and 170 MPa, respectively) [35], regardless of the air or argon conditions. The influence of the ambient conditions during the PMD process involved differences on the mechanical properties between specimens processed in air and in argon, especially in the UTS and YS. It was observed how the average UTS value increased by 9% when specimens were manufactured in air; the YS also showed increments of 13%. Young's modulus and elongation showed similar values, with 161 GPa and 44%, respectively, for specimens processed in air (see Figure 10).

Regarding the effect of the thermal treatment, Figures 11 and 12, the specimens processed in air suffered mild decrements of their UTS, of approximately 7% after TT1 and 10% after TT2. When the specimens were made in argon conditions, their UTS after TT1 and TT2 remained closer, at 446 MPa and 453 MPa, respectively, which means that there was a negligible variation of UTS behavior after the postprocessing treatments when the specimens were performed in argon.

However, the YS values diminished after both treatments. Its tendency remained similar to the as-built specimens and resulted in higher values in air than in argon. Comparing the effect of the heating temperature of the postprocessing treatment: the higher the temperature, the lower the YS measured.

Young's modulus values also presented attenuation with the thermal treatments. These measured lower values after TT2 than after TT1. In this respect, the influence of the two treatments was similar, independently of whether the specimens were fabricated in air or in argon.
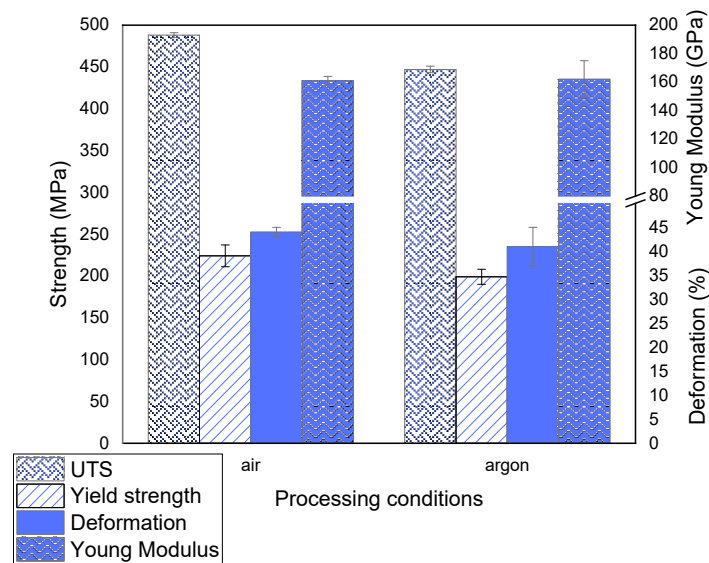
Figure 10. Mechanical properties of PMD as-built specimens vs. the processing conditions of air and argon.
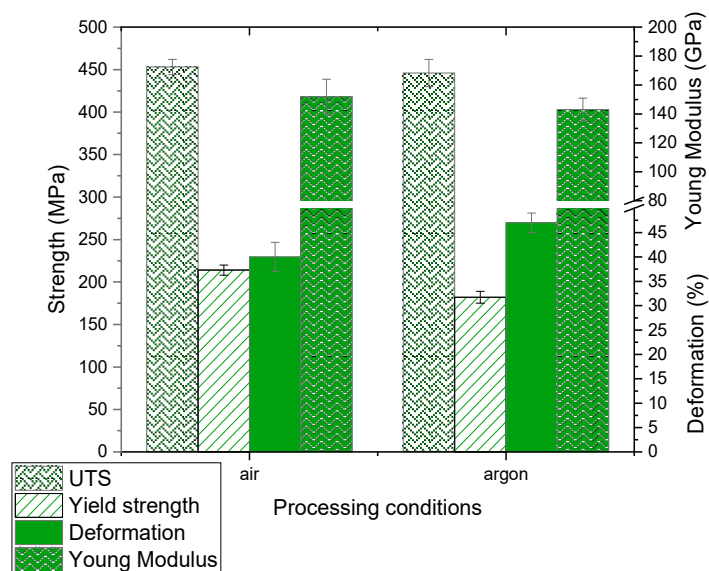

Figure 11. Mechanical properties of PMD specimens after TT1 vs. the processing conditions of air and argon.

On studying the results of the YS behavior, the application of the TT1 led to a decrease of 5% and 9% in specimens manufactured in air and in argon, respectively. Similarly, the TT2 contributed towards reducing the YS by 15% and 18% regarding the as-built specimens. It seems that both treatments more strongly affected the specimens fabricated in argon; in general, TT2 caused a greater decrement in the YS. The Young's modulus values were affected in the same way by each of the thermal treatments.

The deformation of the specimens after each of the thermal treatments varied slightly. In specimens fabricated in argon, the enhancement of the elongation reached from 41% of the as-built specimens up to approximately 47%, after TT1 and TT2. In the case of the specimens manufactured in air, the deformation remained closer to 44% independent of the treatment carried out. Therefore, the effect of the postprocessing was more significant in specimens fabricated in argon.
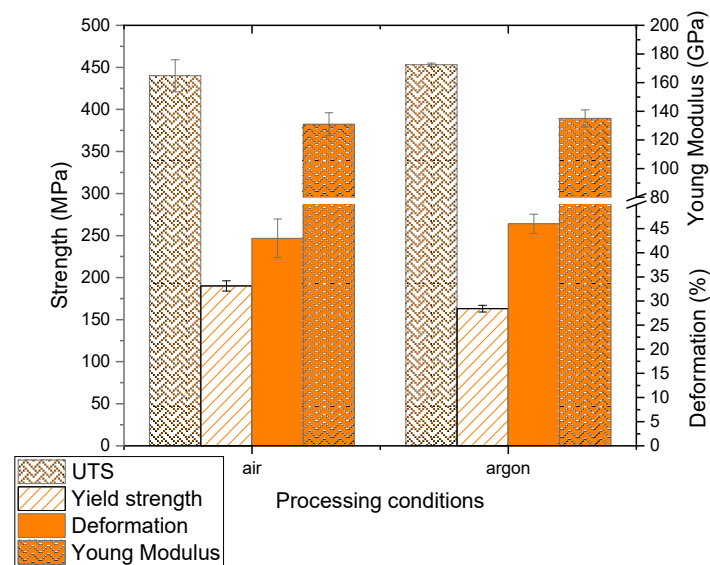
Figure 12. Mechanical properties of PMD specimens after TT2 vs. the processing conditions of air and argon.

In general, it becomes apparent that the YS and Young's modulus present lower values as the heat treatment temperature increases, and therefore these samples offer a lower resistance to permanent plastic deformation.

Tables 4 and 5 show the values of the mechanical properties of each of the measured specimens. In the context of the sample locations in the manufactured wall, there was only a negligible trend among the specimens, with the exception of Young's modulus. Even after the thermal treatments, the variation of these properties considering the sample position remained unclear.

Table 4. Ultimate tensile strength and elongation results for the specimens studied.

	W1 (Built in Air)			W2 (Built in Argon)	
Sample	**UTS (MPa)**	**Elongation (%)**		**UTS (MPa)**	**Elongation (%)**
1.1 as built	491	44	1.1 as built	450	42
1.2 as built	483	45	1.2 as built	442	37
1.3 as built	489	43	1.3 as built	449	44
As built Average	488 ± 3 (0.7%)	44 ± 1 (1.9%)		447 ± 4 (0.8%)	41 ± 4 (8.6%)
ASTM A 240	485	40		485	40
[12]	450	40		450	40
2.1 TT1	465	44	2.1 TT1	465	47
2.2 TT1	451	36	2.2 TT1	448	44
2.3 TT1	444	40	2.3 TT1	426	49
TT1 Average	453 ± 9 (1.9%)	40 ± 3 (8.2%)		446 ± 16 (3.6%)	47 ± 2 (4.4%)
3.1 TT2	416	49	3.1 TT2	461	49
3.2 TT2	440	42	3.2 TT2	442	47
3.3 TT2	463	39	3.3 TT2	455	43
TT2 Average	440 ± 19 (4.4%)	43 ± 4 (9.7%)		453 ± 8 (1.8%)	46 ± 2 (5.4%)

Table 5. Young's modulus and yield strength results for the specimens studied.

Sample	W1 (Built in Air)			W2 (Built in Argon)	
	Young's Modulus (GPa)	Yield Strength (MPa)		Young's Modulus (GPa)	Yield Strength (MPa)
1.1 as built	160	238	1.1 as built	161	205
1.2 as built	159	205	1.2 as built	149	205
1.3 as built	165	230	1.3 as built	176	188
As built Average	161 ± 3 (1.9%)	224 ± 13 (5.8%)		162 ± 13 (8.3%)	199 ± 9 (4.3%)
ASTM A 240	200	170		200	170
[12]		170			170
2.1 TT1	144	218	2.1 TT1	139	190
2.2 TT1	143	205	2.2 TT1	136	183
2.3 TT1	168	218	2.3 TT1	154	173
TT1 Average	152 ± 12 (7.6%)	214 ± 6 (2.9%)		143 ± 8 (5.5%)	182 ± 7 (3.8%)
3.1 TT2	127	196	3.1 TT2	137	168
3.2 TT2	124	193	3.3 TT2	127	162
3.3 TT2	143	182	3.6 TT2	141	159
TT2 Average	131 ± 8 (6.4%)	190 ± 6 (3.2%)		135 ± 6 (4.4%)	163 ± 4 (2.3%)

On observing the Young's modulus results shown in Table 5, the specimens extracted from the central areas of both walls showed lower values than the samples located on the top and the bottom of the walls. This phenomenon was also detected after each of the thermal treatments.

3.3. Microindentation and Wear Behavior

The microindentation tests were conducted in each of the specimens and employed two different maximum loads of 1 N and 5 N; three runs were performed for each load. Figure 13 depicts the P–h curves, loading and unloading, in which the load vs. indentation depth is represented using average values after the tests. Concerning the applied thermal treatments, there were no significant variations in the penetration depth curves. Regardless of the thermal treatment, the penetration was higher in samples processed in argon (Figure 13c,d) than in specimens manufactured in air (Figure 13a,b). This trend is clearly visible under the high applied load.

In Table 6 (1 N) and Table 7 (5 N), values of the elastic recovery, absolute and relative, are listed. In general, the relative elastic recovery was greater in specimens fabricated in argon than in air. It should be borne in mind how as-built specimens and specimens after TT1 fabricated in argon exhibited similar values. However, after TT2 there was an enhancement of the elastic recovery; it can be inferred that the 316L stainless steel became softer than for as-built specimens. Results were more noticeable at five newtons maximum load than at one newton.

Table 6. Elastic recovery values employing a load of 1 N.

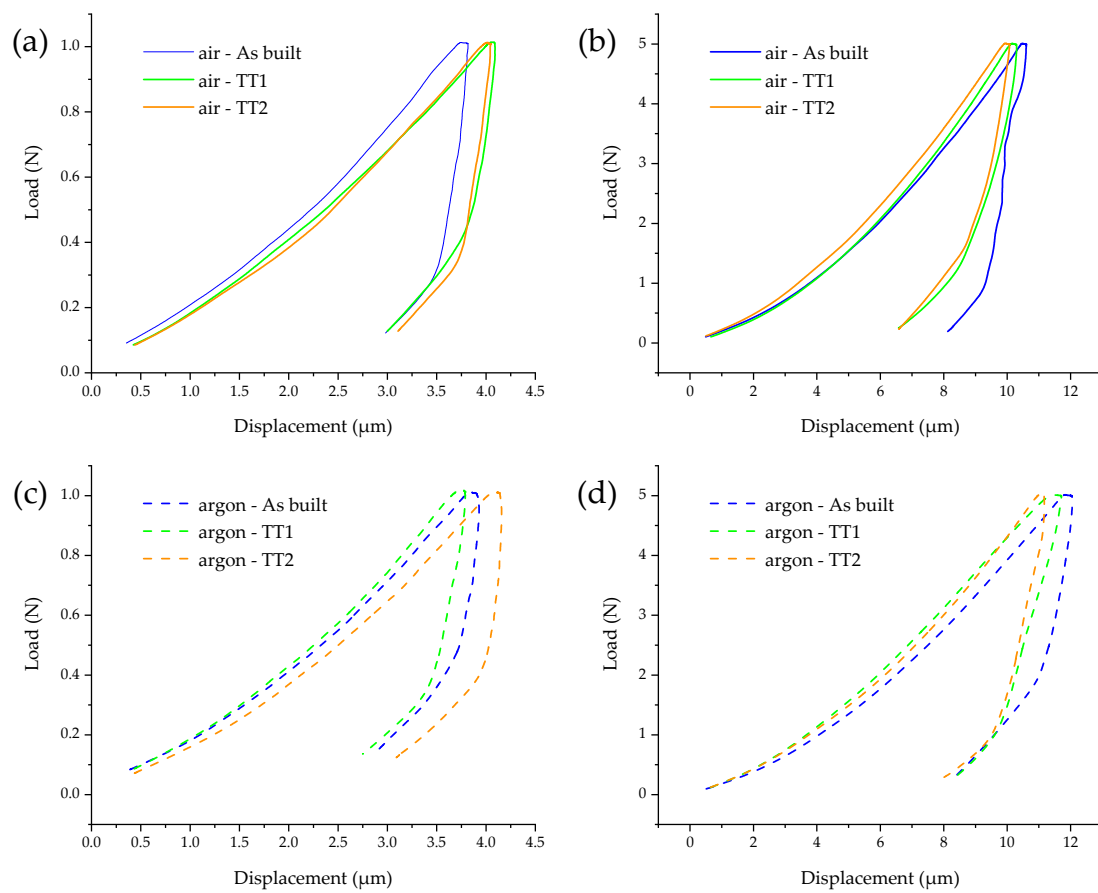| Sample	W1 (Built in Air)			W2 (Built in Argon)	
	Absolute Elastic Recovery (μm)	Relative Elastic Recovery (%)		Absolute Elastic Recovery (μm)	Relative Elastic Recovery (%)
1.1 as built	0.85	22.2	1.1 as built	1.00	26.0
2.2 TT1	1.09	26.7	2.2 TT1	1.08	28.4
3.3 TT2	0.97	23.8	3.3 TT2	1.23	34.3

Figure 13. P–h curves for micromechanical behavior of samples. (**a**) Air atmosphere, 1 N; (**b**) air atmosphere, 5 N; (**c**) argon atmosphere, 1 N; and (**d**) argon atmosphere, 5 N.

Table 7. Elastic recovery values employing a load of 5 N.

	W1 (Built in Air)			W2 (Built in Argon)	
Sample	Absolute Elastic Recovery (μm)	Relative Elastic Recovery (%)		Absolute Elastic Recovery (μm)	Relative Elastic Recovery (%)
1.1 as built	2.37	22.3	1.1 as built	3.04	30.1
2.2 TT1	3.73	36.2	2.2 TT1	3.52	30.0
3.3 TT2	3.55	35.3	3.3 TT2	3.82	36.5

The tribological characterization revealed slight variations on the wear behavior depending on the processing conditions. On observing the resulting coefficient of friction (COF), there was a small increase in specimens processed in argon, as can be appreciated in Figure 14.

Regarding the effect of the thermal treatment on the wear behavior, there was no distinguishable trend. There was an initial stage named accommodation period, in which the COF enhancement sharply took place. Subsequently, a second tranche showed a slight increase, and, finally, the stabilization occurred, which is nearly constant in its variation vs. time [36]. Moreover, as can be observed in Figure 14, the COF suffered a visible rise after 200 s; this enhancement was greater in specimens with a low COF than in specimens with high values thereof. It can be presupposed that such an increase may be related to a possible adhesion mechanism that corresponds to the beginning of the third stage of the curves.
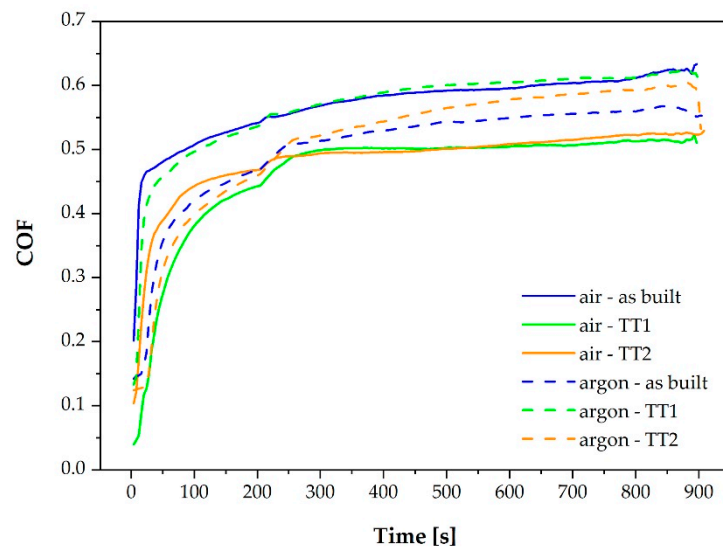
Figure 14. Representation of the coefficient of friction vs. analysis time.

Figure 15 reveals OM images of the worn tracks. Abrasion mechanisms can be appreciated; parallel marks in the same sliding direction can easily be identified. The material removal can clearly be observed as debris in these worn tracks.
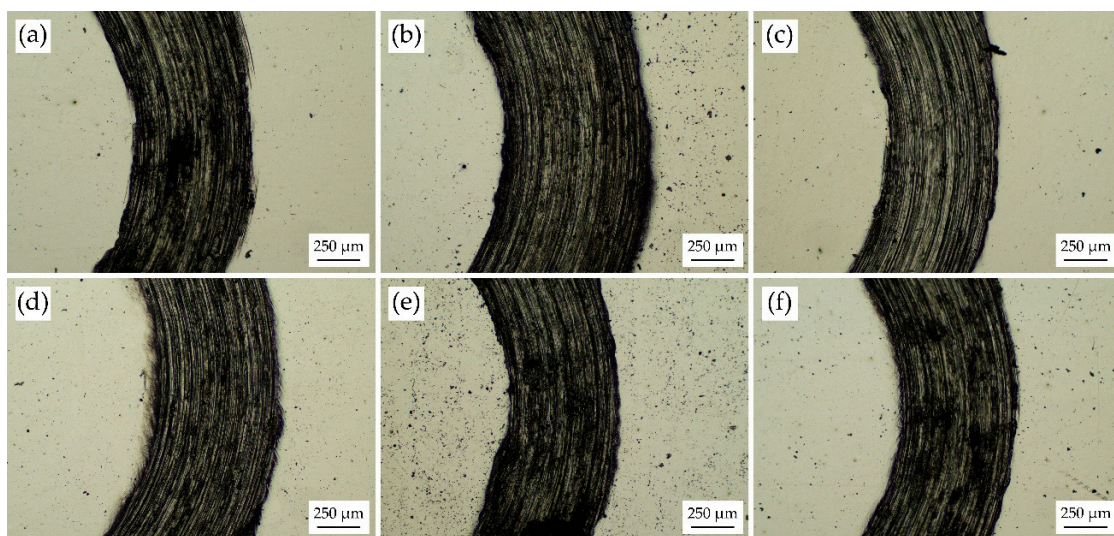

Figure 15. OM images from the worn tracks of the following specimens. (**a**) air-1.1; (**b**) air-2.2; (**c**) air-3.3; (**d**) argon-1.1; (**e**) argon-2.2; and (**f**) argon-3.3.

The worn track areas of the specimens are depicted in Figure 16; these values were calculated by means of the difference between the external and inner circular areas. The tendency was inverse regarding the COF. On comparing the effect of the processing conditions, the values obtained for worn tracks were slightly larger in specimens processed in air than those fabricated in argon. As an additional observation, the influence of thermal treatment was of no significance on the worn tracks, which made difficult to determine a clear trend.

Considering the short period of testing time and distance, in addition to the wear mechanisms that resulted in debris, no significant findings were found regarding the weight loss and the wear rate.
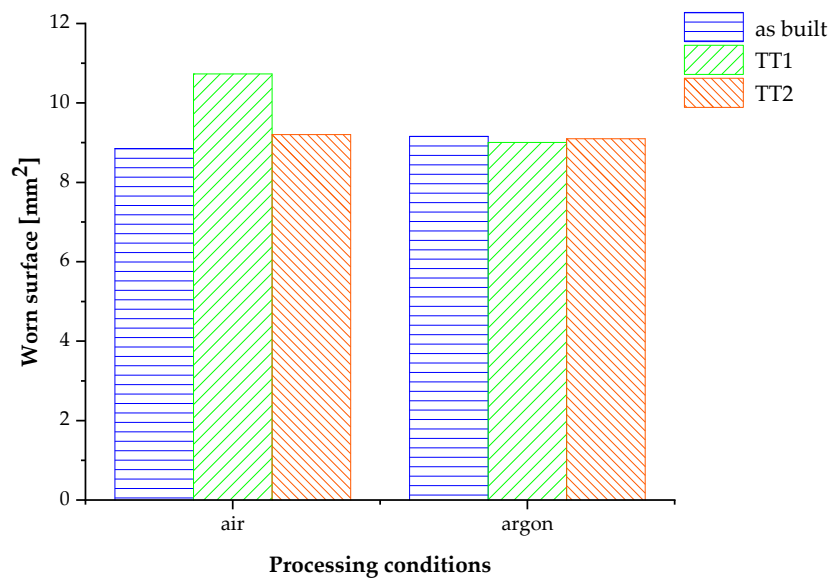
Figure 16. Worn track area values obtained after the tribological tests.

4. Discussion

An austenite (γ) matrix with a retained vermicular ferrite phase (δ) constituted the microstructure of the specimens, regardless of the processing conditions and the thermal treatment.

As previously described, the δ-phase grew as a dendritic morphology. Subsequently, around the boundaries of the ferrite, the austenite phase emerged due to a peritectic transformation during the cooling process with γ oriented within the dendrites.

It was confirmed that the retained δ-phase was rich in chromium and molybdenum. One possible explanation for this composition is related to the inability of these larger and heavier elements to complete their diffusion in rapid solidification since they may have insufficient time to dissolve.

In previous studies regarding the development of 316L stainless steel by AM, in which the built part presented a great height, the analysis of the heat-affected zones showed specimens with significant variations in the ferrite phase morphology depending on the analyzed area [18,25]. In these studies the microstructural evolution started from the top with reticular morphology of the δ phase; it then followed on to a vermicular structure in the center of the wall; and, finally, in the studied microstructure drawn of the base of the built part, this δ phase manifested a fine vermicular structure. Regarding the specimens extracted from the manufactured walls in this research, the observed microstructures revealed only a vermicular morphology and a slight refining trend, particularly in the center of the built part, as can be observed in Figure 6.

Relating the observed microstructure and the study of the macro- and micromechanical and tribological results, the content of the retained ferrite was linked to the properties measured. There were slight variations in the ferrite occurrence in terms of the processing atmosphere. Thus, in specimens manufactured in air, more ferrite could be appreciated and the values of UTS and YS were higher than those manufactured in argon. This retained ferrite phase, located mainly at the grain boundaries [18,32], was responsible for the enhancement of these mechanical properties, regardless of the thermal treatment, making samples stiffer. Other researchers have established that in welded and cast steel, δ phase acts as a strengthener [25]. These differences were less significant when the specimens were postprocessed through thermal treatment.

When specimens were produced in air with a posterior thermal treatment, this led to a decrement of the UTS, YS and Young's modulus. It seems that the effect of the thermal treatment depended on the property evaluated, whereby the changes in UTS more noticeable in air than in argon and the YS, Young's modulus and elongation more affecting in argon than in air. Considering the UTS, the possible appearance of inner porosity, as well as additional microstructural defects, could diminish the UTS

of the specimens manufactured in air. It should be borne in mind that the specimens processed in argon showed results that were more homogenous than specimens fabricated in air. An increase in elongation produced strain-hardening as observed in argon-built specimens [25].

This evolution was also related to the retained ferrite and the austenite phases; when the percentage of austenite phase increased, the deformation of the 316L stainless steel reached higher values. By evaluating how the thermal treatment affected the behavior of the specimens, the main answer was found in the transformation of the ferrite into austenite. TT2 involved heating at 950 °C for two hours, causing not only a possible enlargement of the grain size, but also a diminution of the quantity of ferrite phase. Thus, the TT2 promoted the softening of the materials, which can be inferred from the results of the tensile tests that show lower YS, more elongation and more elastic recovery measured after TT2 than after TT1. Moreover, observing the microstructure, the presence of austenite phase was more notorious in the specimens heated at the highest temperature.

Related to the micromechanical findings, the resulting trend remained unclear. The relative elastic recovery, as well as penetration depth, appeared to be higher in specimens processed in argon than in air. The thermal treatment would enhance this elastic behavior. The presence of the austenite, in addition to less content of the ferrite located at grain boundaries, promoted the softening of the specimen.

At five newtons of maximum load, the results were more evident than at one newton. When loading at five newtons, the indentation seemed to encompass a more comprehensive microstructure response. In contrast, loading at one newtons made the trend unclear. This could be related to the formation of oxide layers during the manufacturing of the specimens. Furthermore, it could be due to the microplasticity phenomenon in local areas that is probably caused by the low load.

According to the determined COF, there was a singular relation between specimens with high elongation and high COF. This fact could be linked to the mechanisms that took place during the tribological test. Therefore, the more deformable the material is, the more shear force and surface roughness appear, as well as the adherence of the loose particles on the worn surface [37]. Furthermore, the greater the deformability of the specimens, the more debris appears which in turn generates a higher COF. A smaller groove width is generated in these specimens due to the adhesion of the debris to the ball, thereby generating instability in the formation of the groove, which is appreciable in the exterior of the worn tracks.

5. Conclusions

The key conclusions are presented in terms of the two main factors of influence studied herein: processing conditions and thermal treatment.

(i)   Processing conditions:

- The influence of the inert atmosphere generated by argon gas promoted slight effects on the microstructure and final behavior of the specimens;
- Relating to the retained ferrite (δ), specimens processed in argon showed a lower content in this phase than specimens manufactured in air. This phenomenon was reflected in the mechanical properties measured in as-built specimens processed in argon;
- The elastic recovery was lower in specimens manufactured in air than in argon;
- The COF presented higher values when the specimens were processed in argon than in air and the results suggested that there were abrasive mechanisms with more debris.

(ii)   Thermal treatments:

- These affected the specimens to a lower degree than expected; the specimens treated at a higher temperature (TT2) suffered a higher variation of their mechanical properties than specimens treated at TT1. Therefore, the higher the thermal treatment temperature, the lower the YS and Young's modulus measured;

- Both thermal treatments resulted in a decrease the vermicular phase. TT2 caused greater transformation of the ferrite (δ) than TT1;
- The relation of the elastic recovery with the thermal treatment was unclear, although TT2 appeared to be more influential in the enhancement of the elastic recovery.

Author Contributions: All the authors have cooperated to obtain high-quality research. Conceptualization, C.A. and E.N.; methodology, I.M.-M., E.M.P.-S. and C.A.; formal analysis, I.M.-M.; investigation, C.A., I.M.-M., E.A. and E.M.P.-S.; resources, M.K.; data curation, E.A. and E.M.P.-S.; writing—original draft preparation, I.M.-M., E.M.P.-S., C.A. and E.A.; writing—review and editing, E.A. and I.M.-M.; visualization, E.M.P.-S. and C.A.; and funding acquisition, E.N., E.A., M.K., I.M.-M. and C.A. All authors have read and agreed to the published version of the manuscript.

Conflicts of Interest: The authors declare no conflict of interest.

References

1. Gibson, I.; Rosen, D.W.; Stucker, B. Post-processing. In *Additive Manufacturing Technologies*, 2nd ed.; Springer: New York, NY, USA, 2015; pp. 346–348.
2. Guo, N.; Leu, M.C. Additive manufacturing: Technology, applications and research needs. *Front. Mech. Eng.* **2013**, *8*, 215–243. [CrossRef]
3. Gideon, N.L. The role rand future of the Laser Technology in the Additive Manufacturing environment. *Phys. Procedia* **2010**, *5*, 65–80.
4. Bartolomeu, F.; Buciumeanu, M.; Pinto, E.; Alves, N.; Carvalho, O.; Silva, F.S.; Miranda, G. 316L stainless steel mechanical and tribological behavior—A comparison between selective laser melting, hot pressing and conventional casting. *Addit. Manuf.* **2017**, *16*, 81–89. [CrossRef]
5. Wong, K.V.; Hernandez, A. A Review of Additive Manufacturing. *ISRN Mech. Eng.* **2012**, *12*, 1–10. [CrossRef]
6. Gu, D.D.; Meiners, W.; Wissenbach, K.; Poprawe, R. Laser additive manufacturing of metallic components: Materials, processes and mechanisms. *Int. Mater. Rev.* **2012**, *57*, 133–164. [CrossRef]
7. Mukherjee, M. Effect of build geometry and orientation on microstructure and properties of additively manufactured 316L stainless steel by laser metal deposition. *Materialia* **2019**, *7*, 100359. [CrossRef]
8. Lervåg, M.; Sørensen, C.; Robertstad, A.; Brønstad, B.M.; Nyhus, B.; Eriksson, M.; Aune, R.; Ren, X.; Akselsen, O.M.; Bunaziv, I. Additive Manufacturing with Superduplex Stainless Steel Wire by CMT Process. *Metals* **2020**, *10*, 272. [CrossRef]
9. Pérez-Soriano, E.M.; Ariza, E.; Arévalo, C.; Montealegre-Meléndez, I.; Kitzmantel, M.; Neubauer, E. Processing by Additive Manufacturing Based on Plasma Transferred Arc of Hastelloy in Air and Argon Atmosphere. *Metals* **2020**, *10*, 200. [CrossRef]
10. Mercado Rojas, J.G.; Wolfe, T.; Fleck, B.A.; Qureshi, A.J. Plasma transferred arc additive manufacturing of Nickel metal matrix composites. *Manuf. Lett.* **2018**, *18*, 31–34. [CrossRef]
11. Savolainen, J.; Collan, M. How Additive Manufacturing Technology Changes Business Models?—Review of Literature. *Addit. Manuf.* **2020**, *32*, 101070. [CrossRef]
12. Najmon, J.C.; Raeisi, S.; Tovar, A. Review of additive manufacturing technologies and applications in the aerospace industry. In *Additive Manufacturing for the Aerospace Industry*, 1st ed.; Elsevier: Amsterdam, The Netherlands, 2019; pp. 7–31.
13. Neubauer, E.; Ariza Galvan, E.; Meuthen, J.; Bielik, M.; Kitzmantel, M.; Baca, L.; Stelzer, N. *Analysis of the Anisotropy of Properties in Titanium Alloys made by Plasma Metal Deposition, Proceedings of the Euro PM2019, Maastricht, The Netherlands, 13–16 October 2019*; European Powder Metallurgy Association (EPMA): Shrewsbury, UK, 2019.
14. Norsk Titanium delivers FAA approved AM part to Boeing. *Met. Powder Rep.* **2017**, *72*, 279. [CrossRef]

15. Ariza-Galván, E.; Montealegre-Meléndez, I.; Pérez-Soriano, E.M.; Arévalo Mora, C.; Meuthen, J.; Neubauer, E.; Kitzmantel, M. *Processing of 17-4PH by Additive Manufacturing Using a Plasma Metal Deposition (PMD) Technique, Proceedings of the Euro PM2019, Maastricht, The Netherlands, 13–16 October 2019*; European Powder Metallurgy Association (EPMA): Shrewsbury, UK, 2019; p. 4348497.

16. Song, R.; Xiang, J.; Hou, D. Characteristics of mechanical properties and microstructure for 316L austenitic stainless steel. *J. Iron Steel Res.* **2011**, *18*, 53–59. [CrossRef]

17. Saboori, A.; Piscopo, G.; Lai, M.; Salmi, A.; Biamino, S. An investigation on the effect of deposition pattern on the microstructure, mechanical properties and residual stress of 316L produced by Directed Energy Deposition. *Mater. Sci. Eng. A* **2020**, *780*, 139179. [CrossRef]

18. Chen, X.; Li, J.; Cheng, X.; He, B.; Wang, H.; Huang, Z. Microstructure and mechanical properties of the austenitic stainless steel 316L fabricated by gas metal arc additive manufacturing. *Mater. Sci. Eng. A* **2017**, *703*, 567–577. [CrossRef]

19. Cherry, J.A.; Davies, H.M.; Mehmood, S.; Lavery, N.P.; Brown, S.G.R.; Sienz, J. Investigation into the effect of process parameters on microstructural and physical properties of 316L stainless steel parts by selective laser melting. *Int. J. Adv. Manuf. Technol.* **2014**, *76*, 869–879. [CrossRef]

20. Fayazfar, H.; Salarin, M.; Rogalsky, A.; Sarker, D.; Russo, P.; Paserin, V.; Toyserkani, E. A critical review of powder-based additive manufacturing of ferrous alloys: Process parameters, microstructure and mechanical properties. *Mater. Des.* **2018**, *144*, 98–128. [CrossRef]

21. Debroy, T.; Wei, H.L.; Zuback, J.S.; Mukherjee, T.; Elmer, J.W.; Milewski, J.O.; Beese, A.M.; Wilson-Heid, A.; De, A.; Zhang, W. Additive manufacturing of metallic components-Process, structure and properties. *Prog. Mater. Sci.* **2018**, *92*, 112–224. [CrossRef]

22. Suryawanshi, J.; Prashanth, K.G.; Ramamurty, U. Mechanical behaviour of selective laser melted 316L stainless steel. *Mater. Sci. Eng. A* **2017**, *696*, 113–121. [CrossRef]

23. Prashanth, K.G.; Scudino, S.; Chatterjee, R.P.; Salman, O.O.; Eckert, J. Additive Manufacturing: Reproducibility of Metallic Parts. *Technologies* **2017**, *5*, 8. [CrossRef]

24. Salman, O.O.; Gammer, C.; Chaubey, A.K.; Eckert, J.; Scudino, S. Effect of heat treatment on microstructure and mechanical properties of 316L steel synthesized by selective laser melting. *Mater. Sci. Eng. A* **2019**, *748*, 205–212. [CrossRef]

25. Chen, X.; Li, J.; Cheng, X.; Wang, H.; Huang, Z. Effect of heat treatment on microstructure, mechanical and corrosion properties of austenitic stainless steel 316L using arc additive manufacturing. *Mater. Sci. Eng. A* **2018**, *715*, 307–314. [CrossRef]

26. ASTM. *A240: Standard Specification for Chromium and Chromium-Nickel Stainless Steel Plate, Sheet, and Strip for Pressure Vessels and for General Applications*; ASTM International: West Conshohocken, PA, USA, 2019.

27. ASTM. *E-8 Standard Test Methods for Tension Testing of Metallic Materials*; ASTM International: West Conshohocken, PA, USA, 2016.

28. Montero Sistiaga, M.L.; Nardone, S.; Hautfenne, C.; Van Humbeeck, J. Effect of heat treatment of 316L stainless steel produced by selective laser melting (SLM). In Proceedings of the 27th Annual International Solid Freeform Fabrication Symposium, Austin, TX, USA, 8–10 August 2016.

29. ASTM. *C373-88: Standard Test Method for Water Absorption, Bulk Density, Apparent Porosity, and Apparent Specific Gravity of Fired Whiteware Products*; ASTM International: West Conshohocken, PA, USA, 2006.

30. Oliver, W.C.; Pharr, G.M. An improved technique for determining hardness and elastic modulus using load and displacement sensing indentation experiments. *Mater. Res.* **1992**, *7*, 1564–1583. [CrossRef]

31. Pasang, T.; Kirchner, A.; Jehring, U.; Azizderouei, M.; Tao, Y.; Jiang, C.P.; Wang, J.C.; Aisyah, I.S. Microstructure and Mechanical Properties of Welded Additively Manufactured Stainless Steels SS316L. *Met. Mater. Int.* **2019**, *25*, 1278–1286. [CrossRef]

32. Wang, C.; Tan, X.; Liu, E.; Tor, S.B. Process parameter optimization and mechanical properties for additively manufactured stainless steel 316L parts by selective electron beam melting. *Mater. Des.* **2018**, *147*, 157–166. [CrossRef]

33. Lanzutti, A.; Marin, E.; Tamura, K.; Morita, T.; Magnan, M.; Vaglio, E.; Andreatta, F.; Sortino, M.; Totis, G.; Fedrizzi, L. High temperatura study of the evolution of the tribolayer in additively manufactured AISI 316L steel. *Addit. Manuf.* **2020**, *34*, 101258.

34. Wang, L.; Xue, J.; Wang, Q. Correlation between arc mode, microstructure, and mechanical properties during wire arc additive manufacturing of 316L stainless steel. *Mater. Sci. Eng. A* **2019**, *751*, 183–190. [CrossRef]

35. ASTM. *A473-15: Standard Specification for Stainless Steel Forgings*; ASTM International: West Conshohocken, PA, USA, 2015; pp. 1–5.

36. Fellah, M.; Labaïz, M.; Assala, O.; Dekhil, L.; Zerniz, N.; Iost, A. Tribological behavior of biomaterial for total hip prosthesis. *Mater. Tech.* **2014**, *102*, 601. [CrossRef]

37. Rominiyi, A.L.; Shongwe, M.B.; Ogunmuyiwa, E.N.; Babalola, B.J.; Lepele, P.F.; Olubambi, P.A. Effect of nickel addition on densification, microstructure and wear behaviour of spark plasma sintered CP-titanium. *Mater. Chem. Phys.* **2020**, *240*, 122130. [CrossRef]